Combustion and Flame 227 (2021) 39–51

Contents lists available at ScienceDirect

Combustion and Flame

journal homepage: www.elsevier.com/locate/combustflame

# Experimental study of concurrent-flow flame spread over thin solids in confined space in microgravity

Yanjun Li[a], Ya-Ting T. Liao[a,*], Paul V. Ferkul[b], Michael C. Johnston[b], Charles Bunnell[c]

[a] Case Western Reserve University, Cleveland 44106, OH, United States
[b] Universities Space Research Association, NASA Glenn Research Center, Cleveland 44135, OH, United States
[c] ZIN Technologies, Middleburg Heights 44130, OH, United States

ARTICLE INFO

*Article history:*
Received 23 July 2020
Revised 24 December 2020
Accepted 25 December 2020

*Keywords:*
Concurrent-flow flame spread
Microgravity combustion
Confined space
Flame-wall interactions

ABSTRACT

Concurrent flow flame spread experiments are conducted over thermally thin solid fuels in microgravity aboard the International Space Station (ISS) under varying levels of confinement. Samples of cotton fiberglass blended textile fabric are burned in air flows in a small flow duct. Baffles are placed parallel to the sample sheet, one on each side symmetrically. The distance between the baffles is varied to change the confinement of the burning event. Three different materials of baffles are used to alter the radiative boundary conditions of the space that the flame resides: transparent polycarbonate, black anodized aluminum, and polished aluminum. In all tests, samples are ignited at the upstream leading edge and allowed to burn to completion. The results show that at low flow speeds (<17 cm/s), the flame reaches a steady state for all tested baffle types and baffle distances. The spread rates and flame lengths at the steady state increase first and then decrease when the baffle distance decreases, resulting in an optimal baffle distance for flame spread. Furthermore, there exists a limiting baffle distance below which the flame fails to spread. It is concluded that the confinement imposed by the baffles accelerates the flow during the combustion thermal expansion and the baffles reflect flame radiation back to the sample surface, both of which intensifying the burning. However, the confinement also limits the oxygen supply and introduces conductive heat loss away from the flame. At the same baffle distance and imposed flow speed, flame length and spread rate are largest for polished aluminum baffles, and lowest for transparent polycarbonate baffles. The differences are most prominent at intermediate tested baffle distances. While the radiative heat feedback from the baffles is expected to increase when the baffle distance decreases, flame length and flame spread rate are similar for all baffle types at small baffle distances as the combustion is limited by the reduced oxygen supply.



## 1. Introduction

Fire safety is of critical importance in aircraft and space vehicles due to limited options to suppress fires and the difficulty to evacuate. To address this, numerous experiments have been carried out to study how flames spread over solid materials in microgravity. These experiments used drop towers [1,2], parabolic flights [3], sounding rockets [4], facilities aboard the International Space Station (ISS) [5], and other space vehicles [6,7]. The previous experiments focused on the effects of environmental conditions (e.g., oxygen percentages, pressure levels, flow velocities) and flow configurations (concurrent or opposed). They provided abundant data regarding the flame structure, flame spread rate, mechanisms for flame spread, and mechanisms for extinctions. For example, a previous NASA project, Burning and Suppression of Solids (BASS) examined the burning processes of various materials (e.g., thin cotton-fiberglass based fabrics, Nomex, Ultem, and PMMA slabs, rods, and spheres) in concurrent and opposed flows using a small flow duct (height: 7.6 cm) operated in the Microgravity Science Glovebox (MSG) aboard the ISS [5]. For the tested cotton-fiberglass fabric samples (referred to as SIBAL), steady flame spread was observed in low-speed concurrent flows (~20 cm/s). The flame length and spread rate increased with flow velocity and ambient oxygen percentage up to about 22% (oxygen is determined by the day-to-day variation in ISS cabin atmosphere and is usually in the range of 21% to 22%). A low-speed quenching velocity was also identified and shown to decrease when the oxygen percentage increased. In another NASA-led project Saffire, large samples of the same cotton-fiberglass fabric were burned in a large flow duct (height:

* Corresponding author.
*E-mail address:* yating.liao@case.edu (Y.T. Liao).

https://doi.org/10.1016/j.combustflame.2020.12.042
0010-2180/

51 cm) inside the pressurized cabin of the unmanned Cygnus ISS resupply vehicle [6]. While steady flame spread was also observed, the flame spread rates at the steady state in Saffire were significantly lower than those obtained in BASS even at the same oxygen percentage and flow rate. The different spread rates were suspected to be due to the different confined conditions introduced by the large and small flow ducts used in these two experiments.

Similar phenomenon was reported in numerical studies [8–10]. Shih and T'ien used a two-dimensional steady Computational Fluid Dynamics (CFD) combustion model to study concurrent-flow flame spread over thin solid samples in a flow duct in microgravity [9]. Their results show that, when the flow duct height decreases, the flame length and flame spread rate first increased to a maximum value, and then decreased. Flow channeling effect (i.e., flow acceleration caused by thermal expansion of the combustion gaseous products in a limited space [9]), restriction of oxygen supply, and heat loss to the duct ceiling were identified as competing factors that resulted in the observed non-monotonic trend of the flame spread rate. Furthermore, when the radiation reflection from the duct walls was considered in the model, converged solutions were not achieved for some simulated duct heights. It is suspected that the flame may be continually growing in these confined conditions and this transient process could not be captured by the pseudo steady time independent model used at the time. Li et al. [10] conducted a three-dimensional transient numerical study and considered the geometry of the BASS experiments. In their work, the duct height was varied between 1 and 9 cm to investigate the effects of the flow confinement on flame spread. The results predicted that the optimal duct height for fastest flame spread in a 10 cm/s air flow was 4 cm. Above this optimal duct height, the flow confinement affects the flame spread process mainly through the flow channeling effect as the heated gases expand. The flame spread rate varies approximately inversely with the duct height [10] in this regime. Below the optimal duct height, the flame spread rate is proportional to the oxygen supply to the combustion zone and the spread rate is approximately linearly proportional to the duct height [10].

Nakamura et al. [11] used a time dependent model to study the effect of ignition and flame spread under confined conditions with externally forced radiation in support of a microgravity experiment [12]. These two works began ignition in the center of a thermally thin fuel, leading to mostly opposed flame spread into the fresh oxidizer stream. Some concurrent flame spread occurred immediately after ignition, before the opposed flame grew large enough to shield the downstream concurrent flame from fresh oxidizer.

In normal gravity, previous experiments also showed that fires in confined spaces (e.g., parallel panels, channels) can be longer and spread faster compared to fires in open spaces [13–15]. Shih and Wu [13] performed upward flame spread experiments over parallel thin paper sheets. When the distance between the paper sheets is larger than 10 cm, fire behavior is similar to that of one single sheet. As the separation distance between the paper sheets decreases, the adjacent flames begin to interact with each other and flame spread rate increases. It was concluded that both the chimney effect due to buoyancy and the radiation interactions between the adjacent flames and samples intensify the fires. However, when the separation distance is further reduced, flames between parallel samples suffer from oxygen depletion and the flame spread rate decreases. Similar non-monotonic trend of flame spread rate was also observed by Zhu et al. [15]. In their studies, the effects of the spacing between a wall and a solid fuel on upward flame spread behaviors were investigated, using 1mm-thick PMMA fuel samples. They predicted the maximum flame spread rate and mass-loss rate occurred at a spacing of ~6.5% of the wall height due to the enhanced radiation flux incident on the PMMA surface.

In microgravity, Olson conducted concurrent-flow flame spread over three parallel thin fuel sheets, using NASA Glenn Research Center's 5.18 s Zero Gravity Research Facility [16]. The distance between the sheets varied from 1.27 cm to 3.31 cm. At 5 cm/s concurrent flow, the optimal gap spacing between sheets for the flame spread rate is found to be ~ 3.2 cm: the flame spread rate increased to 1.5 times the single sheet value. It was concluded that the radiation exchange augments the flame heat flux to the fuel surface, enhancing the burning. Many other works exist varying the level of externally forced radiation on concurrent [17,18] and opposed flame spread [3]. Other experiments limit the amount of oxidizer to the flame zone in microgravity by reducing oxygen concentration or forced flow velocity [5–7]. Some studies vary the amount of flame confinement in an attempt to suppress buoyancy flow as a sort of 'simulated' microgravity [19–23]. The experiments were found to mostly agree with microgravity experiments in the opposed flow direction. However, to the authors' best knowledge, there are no published works that specifically investigate the effects of confinement on concurrent-flow fire behavior in long-duration actual microgravity.

In the work presented in this paper, the previous BASS hardware [5] is refurbished and modified to allow different levels of flow confinement and different radiative wall reflection boundary conditions. A series of microgravity experiments (referred to as Confined Combustion) are carried out aboard the ISS. The aerodynamic and radiative interactions between a flame and its surrounding walls and the fate of the flame (no ignition, growing flame, steady flame, or extinction) are explored systematically for various confined conditions. One benefit of conducting thermal fluid (including combustion) experiments in a microgravity environment is the removal of the confounding factor of gravity-induced buoyancy flow. This facilitates the observation of the underlying physics of the burning events. While the findings of this study can be directly applied to space applications, a major goal is to provide guidance for future structural design and improve fire safety code and response for both space and Earth applications.

## 2. Microgravity experiments

### 2.1. Experiment apparatus

The experimental setup is shown in Fig. 1. The experiment is based on the existing flow duct hardware from BASS [5]. The flow duct is 20 cm long and has a square cross-section 7.6 cm × 7.6 cm. Flow velocity ($U_\infty$) is measured by a built-in air velocity transducer (TSI$^{TM}$ # 8475) positioned in the fan section (see Fig. 1b) between the flow straightener and the duct inlet screen. The flow duct is capable of providing flow up to 55 cm/s [24]. The duct operates in the Microgravity Science Glovebox (MSG) used for work volume isolation aboard ISS. Along with ISS environmental sensor data, an $O_2$ sensor (Quantek model 201 accuracy +/−2% of reading) is installed in the MSG to monitor the oxygen consumption during each test. A high-resolution video camera is used to record the burning events from the top window (sample edge view) of the flow duct. The spatial resolution and the frame rate of the video recordings are 12.5 pixels/mm (or 0.08 mm/pixel) and 24 frames per second (or ~ 42 ms/frame) respectively. The camera is set to auto adjust for white balance, exposure, and digital gain. An ISS laboratory camera downlink was occasionally used for a secondary view, normal to the fuel surface (when transparent or no baffles were used), through the MSG front window.

In this work, a new baffle/sample system is developed (Fig. 2). Similar to BASS, each sample is held in position sandwiched between two stainless steel sample frames with black oxide surface

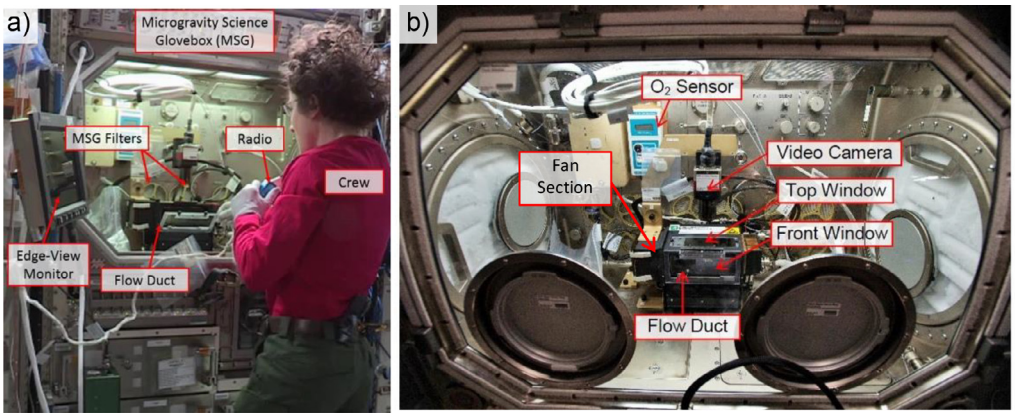


**Fig. 1.** Experimental setup in the Microgravity Science Glovebox (MSG) aboard the International Space Station. A sealing front window for containment and a cloth light cover are installed over the MSG work volume before each test run. a) ISS crew member sets up and performs each test while in real time space to ground communication with the science team in the Glenn research center ISS Payload Operations Center (GIPOC). b) Close-up view of the experimental setup.

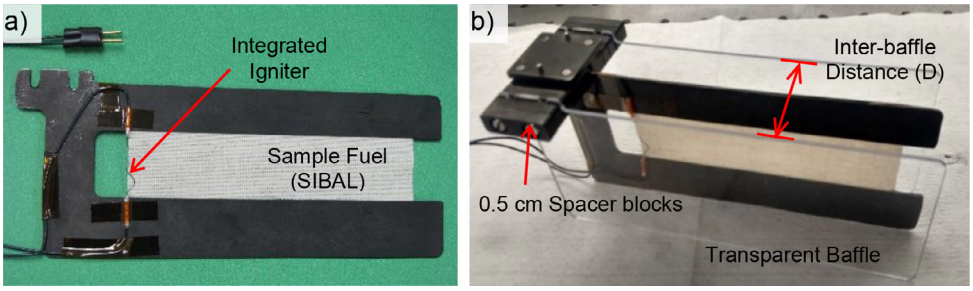


**Fig. 2.** a) Sample frame with fuel and igniter. b) Assembly of the sample/baffle carrier, sample frame, and two parallel transparent baffles. The distance of the fuel to either baffle is D/2.

treatment (Fig. 2a). The sample frame is 13.8 cm long and 6.1 cm wide and the exposed sample surface is 10 cm long and 2.2 cm wide. A 29-AWG Kanthal hotwire in a sawtooth pattern with resistance ~ 1 Ω (powered at about 3.7 A) is located at the leading edge of the sample to serve as the igniter. The sample frame is then placed at the center position of a mounting system, together with two parallel flat baffles (Fig. 2b), one on each side of the sample symmetrically. The mounting system consists of a series of 0.5 cm spacers. By controlling the number of spacers between the baffles and the sample, different levels of flame confinement are achieved. The variation of the inter-baffle distance in the flow direction is measured to be within 3% in all cases. A transparent top window is custom-designed to retrofit the BASS flow duct and the baffle/sample assembly is magnetically attached to a mount integrated with the new top window. This mounting system was designed in a way that the sample can be positioned exactly in the middle of the flow duct when the baffle/sample assembly is mounted on the top window.

In Confined Combustion, tested sample materials include SIBAL fabric (75% cotton, 25% fiberglass, see Fig. 2a) and 1mm-thick cast PMMA slabs. Both materials were previously tested in BASS [5] and in various other microgravity experiments [6]. The thin SIBAL fabric facilitates the observation of steady flame spread over cellulose-based materials. The fiberglass matrix retains the sample structure (no curling or breaking on burned sample surface) while cotton burns. The PMMA slabs represent polymeric materials where solid burnout occurs slightly slower (compared with the thin SIBAL fabric). Both materials are commonly used in space vehicles and in earth applications.

In addition to the sample/baffle arrangement described above (sample in the center and two baffles symmetrically on the two sides), the designed mounting system can accommodate a variety of sample/baffle setups. The baffles and the sample frame can be placed at any positions on the rack. The mounting system can also accommodate multiple sample frames and allows burning of parallel sample sheets (similar to Olson's work [16]) in one test. This arrangement allows the study of how one burning sample ignites another and how fires of adjacent samples interact with each other. In this paper, selected data from the SIBAL fuel tests are presented. Data for PMMA and for burning of parallel sample sheets will be reported in separate papers.

Three types of baffles are used: transparent polycarbonate, black anodized aluminum, and reflective polished aluminum (Fig. 3). The reflective baffle (polished aluminum) and the black baffle (black anodized aluminum) are made of 6061 aluminum alloy. To obtain the desired surface radiative properties, the reflective baffle is polished with progressively higher grits to a mirror finish. The black baffle is blasted into a matte finish and anodized black. The surface properties of each baffle are characterized on the ground prior to the experiments. For black and reflective baffles, the specular reflection gloss levels are tested using Konica Minolta Multi Gloss 268A glossmeter at three measurement angles, 20°/60°/85° The values for the reflective baffles are 1300, 670, and 130 GU (gloss units) at the three tested angles respectively, and the values for the black baffles are 0, 0.3, and 1.3 GU respectively. Note that these reflectance measurements only characterize visible light reflectance. A fraction of flame radiation is reported in the infrared range (e.g., at wavelength 2500–3000 nm from $H_2O$ and $CO_2$, and at ~ 4400 nm from $CO_2$ [25]). In 500–2500 nm range, polished aluminum surface is reported with a fairly constant reflectance around ~ 0.95 while the raw surface is around 0.8–0.9 [26]. The reflectance of blasted black anodized aluminum increases from below 0.10 to ~ 0.35 at 700–1200 nm and maintains constant throughout 2500 nm [27].

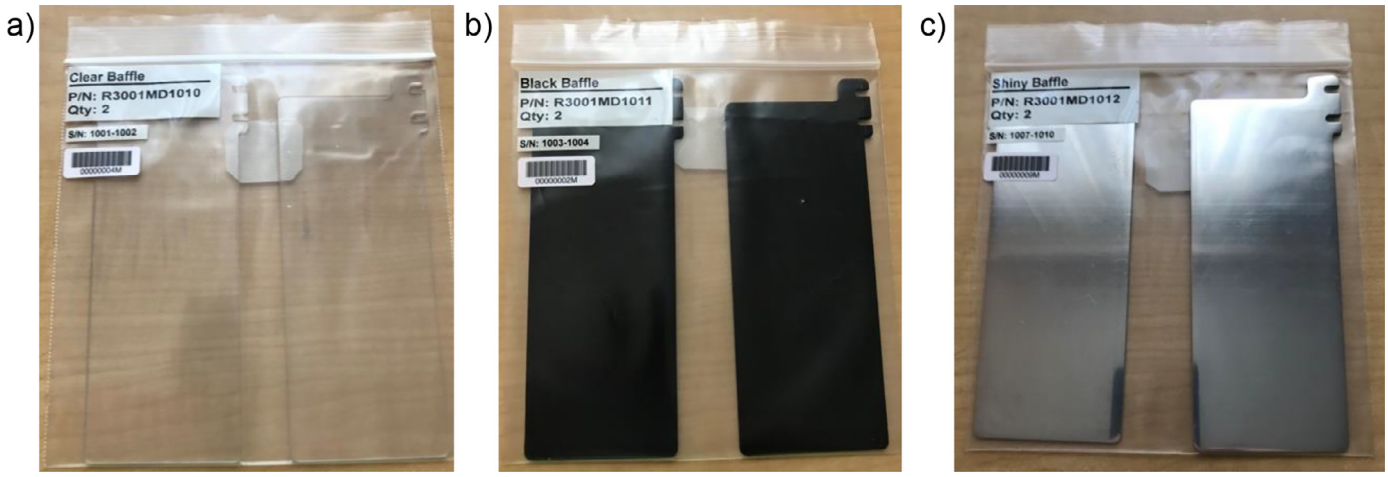


**Fig. 3.** Three types of baffles. a) Transparent polycarbonate. b) Anodized black aluminum. c) Polished aluminum.

The visibly transparent baffles are made from 1.6-mm-thick clear polycarbonate (Makrolon® GP). The transparency is tested using a 5500 K color temperature white light LED (Lightspeed Technologies, HPLS-36, High Powered Light Source w/ 5500 K White LED) and a UV-enhanced silicon photodiode detector (Newport, 818-UV/DB, spectral range: 200–1100 nm) with an accompanying Power/Energy Meter (Newport, 842-PE). The baffle is inserted between the light source and the broadband photodetector. Baseline tests are also performed without any baffles. The differences between the measurements with and without baffles are used to determine the transmittance of the baffles. This measurement is repeated three times and the average transmittance is 92.5% for the polycarbonate baffles. The tested spectrum range is mainly in the visible light wavelengths. The flame radiation in the infrared range is generally less transmissive. Based on the manufacture's data [28,29], the transmittance for a 1 mm-thick polycarbonate remains fairly constant at ~ 90% for wavelength 400–1600 nm, drops to ~40% at 1650 nm, and increases back to 80% at 1750–1950 nm. Further testing is warranted to obtain information of the transmittance at higher wavelengths.

During the experiment operations, real time space to ground communication and live video downlink is established between ISS crew and the science team in the Glenn research center ISS Payload Operations Center (GIPOC). After the flow is established, ignition current is powered on and lasts until the sample ignites and an established flame is observed. The ignition and flame development processes are monitored in real time and recorded using a video camera of the sample edge view through the flow duct top window (Fig. 1b). Post-burn sample images are also obtained.

In all tests, the pressure and oxygen percentage in the MSG remain constant at ISS ambient values of 1.0 atm and ~22% respectively. The daily variation of oxygen concentration in MSG is between 21.3% and 22.9%. Imposed flow velocities range from 5–28 cm/s.

### 2.2. Preflight cold flow characterization

Prior to the ISS operations, cold (i.e., without combustion) flow characterization was performed for the BASS flow duct with the new sample/baffle assembly. The purpose was to evaluate how the sample/baffle assembly may alter the flow profiles. To achieve this, anemometers (Schiltknecht ThermoAir3, precision of 1 cm/s) were placed on the mid-plane between one of the baffles and the sample at three different streamwise locations (near the entry, at the center, and near the exit of the flow duct). Local flow velocities were obtained at these locations at different imposed flow velocities ($U_\infty$ = 3–32 cm/s) and different baffle configurations ($D$ = 2, 3, 4, and 5 cm). Imposed flow velocities were measured by the built-in air velocity transducer in the fan section near the duct inlet.

The results show that the cold flow accelerates slightly in the streamwise direction, possibly due to the buildup of the viscous boundary layers on the surfaces of the baffles and the sample. However, the variation is minimal (see Fig. 4a for results for $D$ = 5 cm). For all tested baffle configurations and imposed flow speeds, the streamwise flow variation is less than 10% from the mean value.

However, with the same flow speed imposed at the duct inlet, the flow in the confined region (i.e., between the baffles and the sample) can vary significantly with the baffle configuration. In this work, effects of confinement on the flame spread process are discussed using microgravity data at $U_\infty$ = 6 cm/s (in Sections 3.3 and 3.4). Figure 4b shows how the local flow at the duct center ($U_c$) varies with the baffle configuration at this imposed flow velocity. Note that in the preflight cold flow characterization, data were obtained at $U_\infty$ = 5 and 7.5 cm/s (see Fig. 4a). Interpolation between these two imposed flow speeds was applied for data in Fig. 4b. The measured flow in the center of the confined region is accelerated ($U_c > U_\infty$) when $D > 2$ cm and decelerated ($U_c < U_\infty$) when $D < 2$ cm.

Figure 4b also shows the anemometer readings for a higher imposed flow speed at 20 cm/s. At this imposed flow speed, $U_c$ also decreases with the baffle distance. However, the variation (percentage-wise) between different baffle settings is smaller compared to that at the lower imposed flow speed.

When the imposed flow encounters the sample/baffle assembly, it redistributes into four pathways (see Fig. 5), I and IV between the baffles and the duct inner walls and II and III between the baffles and the sample. The flow rate in each pathway varies so that the pressure drop due to friction is identical at each pathway. When approximating each pathway as two-dimensional flows between parallel plates, the fully developed flow profile in pathway $i$ can be described as:

$$\frac{u_i}{U_{0i}} = \frac{3}{2}\left(1 - \left(\frac{y_i}{h_i/2}\right)^2\right) \tag{1}$$

Here, $h_i$ is the pathway height (e.g., $h_{II} = h_{III} = D/2$), $y_i$ is the distance to the mid-plane of the pathway $i$, and $U_{0i}$ is the averaged flow speed in each of the pathways. Note that $U_{0i}$ can be different from the imposed flow speed, $U_\infty$, depending on the baffle configurations.

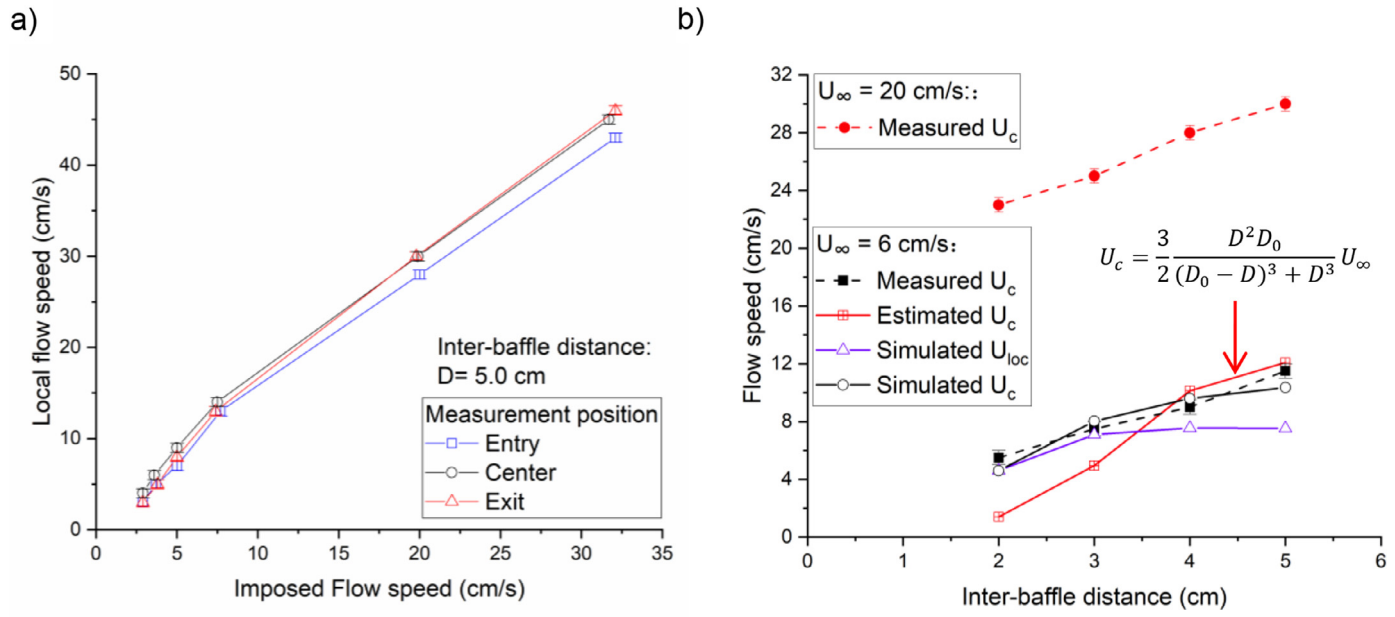


**Fig. 4.** Pre-flight flow characterization. a) Measured flow velocities in the confined region (between the baffle and sample) at different streamwise locations and different imposed flow speeds. $D$ = 5 cm. b) Measured and estimated flow velocities at the center of the confined region at different inter-baffle distances. $\boldsymbol{U}_\infty$ = 6 cm/s. The measurements are interpolated between data at $\boldsymbol{U}_\infty$=5 and 7.5 cm/s. Error bar denotes the anemometer precision.

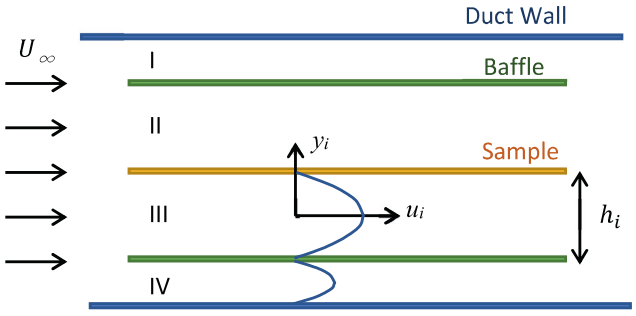


**Fig. 5.** Illustration of two-dimensional idealization of flow pathways for the sample and baffle assembly.

For two-dimensional steady Poiseuille flow, the pressure drop between parallel plates can be expressed as:

$$\Delta p_i = -\frac{3\mu L}{h_i^2} U_{0i} \tag{2}$$

Where $L$ is the length of the parallel plates and $\mu$ is the flow viscosity.

Assuming the pressure drops are the same in all pathways, the incoming flow is redistributed according to the pathway heights: $U_{0i} \propto h_i^2$. Based on Eqs. (1) and 2, the cold flow speed at the mid-plane between one baffle and the sample in the fully developed region can be calculated as:

$$U_c = \frac{3}{2}\frac{D^2 D_0}{(D_0 - D)^3 + D^3} U_\infty \tag{3}$$

Here $U_\infty$ is the imposed flow speed at the duct inlet, $D$ and $D_0$ are the inter-baffle distance and the flow duct height, respectively. The estimated flow speeds are compared to the measurements of the center anemometer (located 10 cm away from the duct inlet) in Fig. 4b. The estimated flow speed decreases when the baffle distance is reduced. This is consistent with the trend of the measured flow speeds.

The deviation of the estimated flow speed from the measurement is suspected to be due to the validity of the assumption of fully developed flow profile (Eq. (1)). The hydrodynamic entrance length for laminar flow between parallel plates can be estimated as $0.02ReH$ [30], where $H$ is the distance between the parallel plates and $Re$ is the Reynold number. For $H$ = 2.5 cm, $U_\infty$ = 6 cm/s, the entrance length is ~5 cm, the same order of magnitude of the sample/baffle length. The flow is likely to be still developing at the end of the flow pathway. Nevertheless, Fig. 4b shows that Eq. (3) roughly captures the center anemometer readings in the cold flow characterization, suggesting that friction on the sample and baffles contribute significantly to the variation of the flow at different baffle distances.

To further characterize the flow profile in the duct, CFD simulations were performed using ANSYS Fluent. The simulations consider $U_\infty$ = 6 cm/s at four different inter-baffle distances. The steady state flow profiles of all cases are included in the Appendix. The simulated local flow speeds at the center anemometer location (i.e., $U_c$) are shown in Fig. 4b. It shows that the simulations match the measurements reasonably well. The simulation results were also used to estimate the local flow speeds the flame may encounter in the experiment. Figure 4b shows the simulated flow speeds 0.5 cm away from the sample surface ($U_{loc}$). Note that this location is chosen based on the observed flame distance from the sample surface (as will be shown later). Similar to $U_c$, $U_{loc}$ decreases with the inter-baffle distance. However, the variation is less significant.

### 2.3. Image analysis

A typical flame image obtained in this work is shown in Fig. 6a. In this figure, the camera line of sight is parallel to the sample surface (edge-view) and the image was taken through the top window of the flow duct (see Fig. 1b).

To quantify the flame development process, a custom code was developed to track the flame locations in each video frame. The flame images are first transformed into gray scale (Fig. 6b) to obtain the information of the flame luminance. The gray-scale

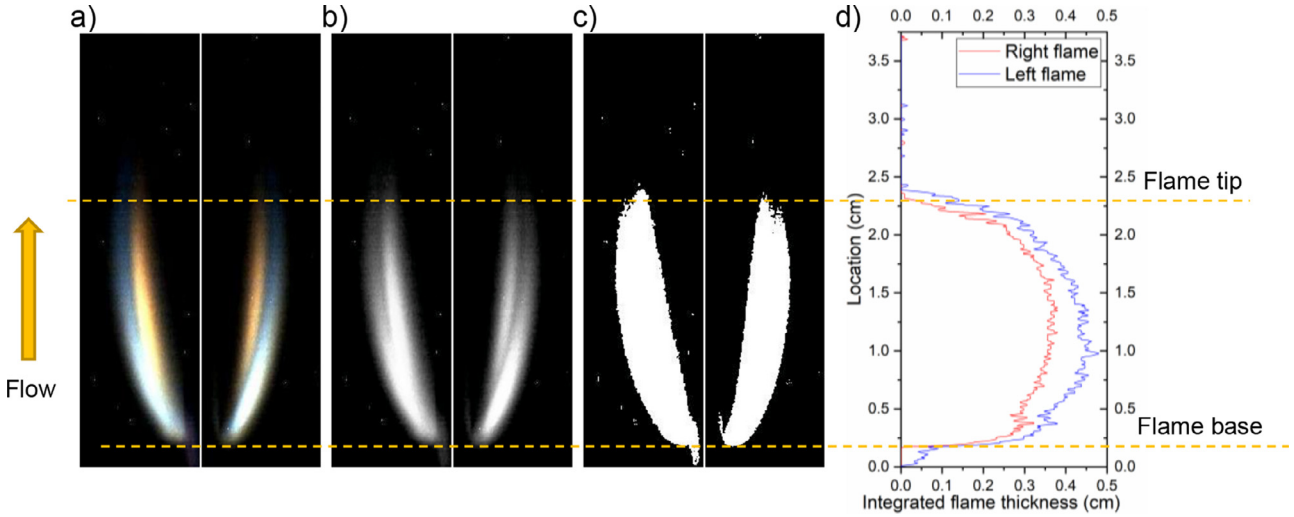


**Fig. 6.** Image analysis and flame position determination. a) Original flame profile. b) Gray scale flame profile. c) Black and white binary flame profile. d) Integrated (along the cross-stream direction) flame thickness versus streamwise location.

images are then transformed into black and white binary (Fig. 6c) with a constant threshold. Finally, the binary flame profiles are analyzed and the integrated (along the cross stream direction) flame thicknesses are determined for flames on each side of the sample (Fig. 6d). Note that the flame thickness varies in the stream direction and the maximum value occurring at the middle portion of the flame is at ~0.4 cm. Also note that the profiles of the flames on the two sides of the sample are fairly symmetric, except that in Fig. 6d the right flame (close to the duct front window) is slightly thinner than the left flame. However, this is not consistent throughout the test or between different tests.

A constant threshold value (0.024 cm) of the flame thickness is used to determine the downstream flame tip and upstream flame base locations. This non-zero threshold value is somewhat arbitrary but was chosen to filter out background noise in the flame images and was shown to correlate well with the flame size obtained by manual examination of the flame images. Overall, the flame tip and base locations of the left and right half of the flames are similar in all image frames (once again, demonstrating the symmetry of the flame profiles).

## 3. Results

The test matrix is summarized graphically in Fig. 7. While the baffle distance, imposed flow velocities, and baffle types are varied, different flame behaviors are observed. At low imposed flow velocities ($\boldsymbol{U}_\infty = 5$–$6$ cm/s), steady state flame spread is observed except for the smallest tested inter-baffle distance ($D = 1$ cm). Under these low-speed flows, samples are ignited at the smallest tested inter-baffle distance but the flame does not spread away from the ignition region. The flame extinguished when the ignition power was off, regardless of the baffle types. When the imposed flow rate is higher ($\boldsymbol{U}_\infty \geq 17$ cm/s), the flame continually grows and does not reach a steady state except when the inter-baffle distance is small ($D < 3$ cm). Note that this observation might be specific to the tested sample length. It is possible that the flame will eventually reach a steady state at these conditions if given a longer duct and sample length. The transient development processes of a steady spreading flame and of a growing flame are presented using two representative cases below.

### 3.1. Steady state flame spread

Figure 8 shows a typical process of flame development leading to a steady spreading state. In this case, the sample is placed between two black baffles with 5.0 cm inter-baffle distance. The imposed flow velocity is 6 cm/s.

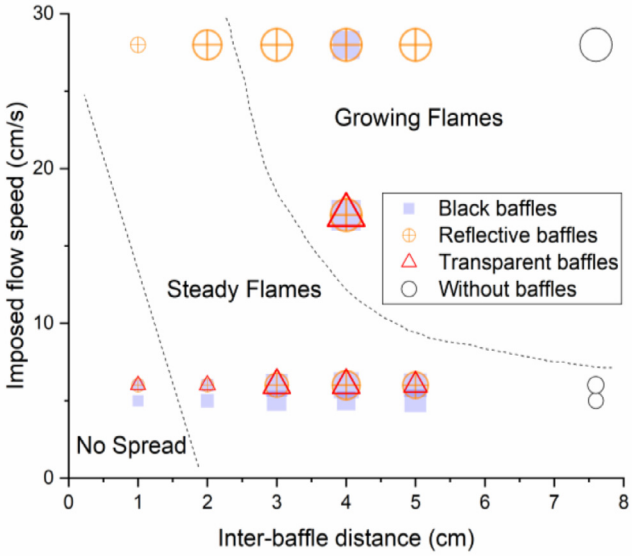


**Fig. 7.** Test points for SIBAL samples in Confined Combustion. The size of the data points (not to scale) denotes the flame spread rate at the steady state (if achieved).

Figure 8a shows a montage of the edge-view images of the flame (baffles are outside of the cropped frames and not shown) and Fig. 8b shows the flame tip and base locations versus time. In the initial frames, the igniter is bright illuminating the interior of the flow duct (and hence the developed code was not able to track the flame locations). After the igniter is de-energized, Fig. 8b shows that the flame quickly reaches a limiting length and steady spread rate. In this work, for all steady state tests, flame spread rate is taken as the slope of the least-squares linear fit through the flame tip and flame base data when the flame base is located in the center region of the sample (between 4 and 7 cm in Fig. 8b). Flame length (difference between flame tip and base locations) is determined in the same time duration. In the representative test, the difference between the flame tip and flame base spread rates are ~ 2.2%. A quasi-steady flame spread is maintained until the sample is fully consumed at which point the flame goes out.

Near the end of the test, when the flame tip reaches the downstream open end of the sample, the flame tip accelerates, the

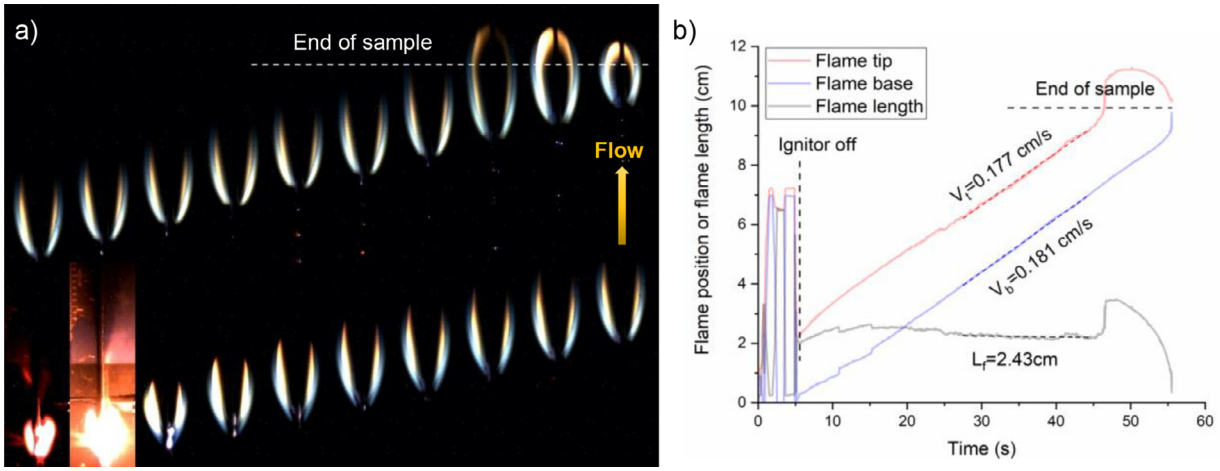


**Fig. 8.** Flame development leading to a steady spreading state. The imposed flow speed is 6 cm/s. Confined conditions: black anodized aluminum baffles with 5.0 cm inter-baffle distance. (a) Montage of edge-view images. Ignition is at lower left and images are 2.8 s apart from left to right, bottom row to top row. (b) Flame locations (the more downstream tip and base among the left and right flames) and flame length versus time.

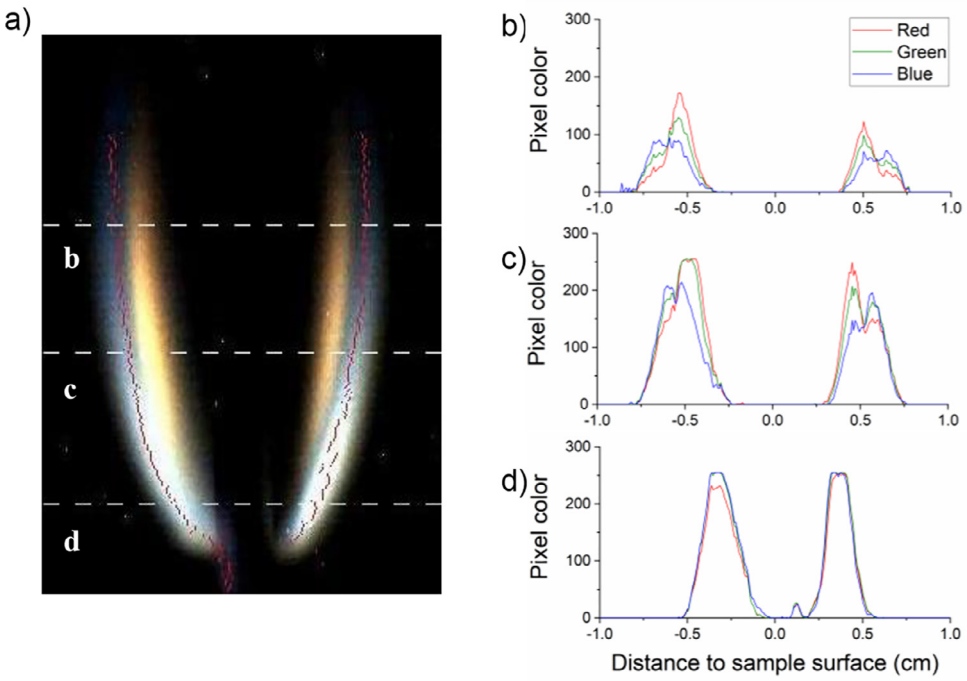


**Fig. 9.** Typical steady state flame profile at low speed flows ($U_\infty$ < 17 cm/s). (a) Flame image. (b)-(d) RGB pixel intensity at three different streamwise locations.

flame suddenly lengthens, and the left and right flames merge at the downstream end. Several edge effects may contribute to this. When the flame spreads along the fuel surface, the gaseous fuel pyrolyzate needs to diffuse across the flow viscous boundary layer to meet with the oxygen in the flow stream. Thus the flame profile resembles the shape of the flow boundary layer [1]. At the downstream trailing edge of sample, the no slip condition ends due to absence of the solid fuel and a gradient-free symmetry plane condition begins. Consequently, the gaseous fuel and hence the reaction zone from each side of the sample can join up. The sudden removal of the no-slip boundary condition leads to increased flow speed near the center plane downstream of the sample fuel. Furthermore, the baffles end near this location (see Fig. 2b). The downstream portion of the flame is no longer subjected to the confinement (less oxygen limitation and conductive heat loss to the baffles). The higher flow speed, additional oxygen supply, and reduced heat loss to baffle and fuel surface contribute to the acceleration of the flame tip near the end of the test.

In this representative test (and in all tests with imposed flow speeds < 17 cm/s), flame exhibits clearly two layers: a thin yellow layer of soot facing the sample surface and a thicker outer blue layer near the two baffles. The RGB pixel values across the flame thickness at three different stream locations are plotted in Fig. 9. The upstream flame base (Fig. 9d) does not show obvious soot zone. All three colors peak at similar cross-stream locations (~0.3 cm away from the sample surface). The center portion of the flame (Fig. 9c) clearly shows different locations for red and blue peaks, reflecting the soot and flame layers. Near the downstream flame tip (Fig. 9b), the combustion zone is predominantly red, suggesting mostly soot. It is suspected that the observed formation of soot is due to insufficient oxygen supply in the inner side (facing the sample surface) and downstream region of the flame. It is also possible that the temperature of outer flame layer is lower than

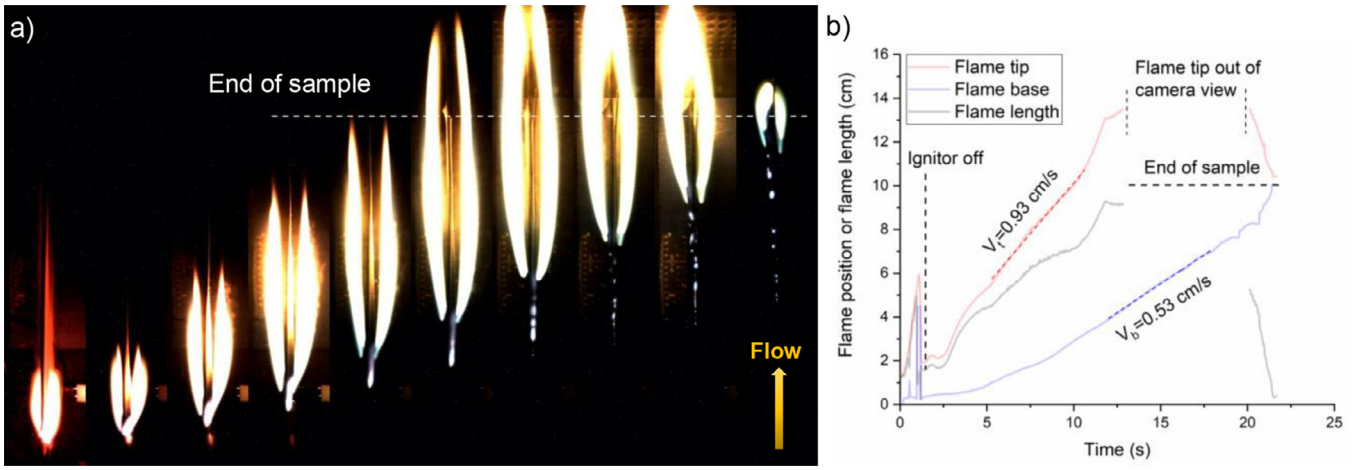


**Fig. 10.** Flame spread of a growing flame. Imposed flow velocity: 28 cm/s. Confined conditions: polished aluminum baffles with 5.0 cm inter-baffle distance. (a) Montage of edge-view images. Ignition is at lower left and images are 2.3 s apart, left to right. (b) Flame locations (the more downstream tip and base among the left and right flames) and flame length versus time.

that of inner layer because of heat loss to the baffles and/or to the flow stream. This can potentially prohibit the formation of soot as well.

To fairly compare the flame profile and flame standoff distance with images of different auto-adjusted camera settings, the most luminous pixel locations are extracted from the blue flame zone (marked by red in Fig. 9a). This represents the flame sheet profile for each test at the steady state.

### 3.2. Accelerating flame spread

The flame spread process of a growing flame is presented in Fig. 10. In this case, the sample is placed between two polished aluminum baffles with 5.0 cm inter-baffle distance. The imposed flow velocity is 28 cm/s. After the igniter is de-energized, the flame tip spreads downstream rapidly and reaches the exit of the flow duct. The flame base accelerates while spreading downstream with a smaller spread rate compared with the flame tip. The spread rates of the flame tip and the flame base are evaluated in Fig. 10b. For the flame base, the spread rate is calculated using the same criteria (i.e., when the base is between 4 and 7 cm) as for the steady cases. For the flame tip, the spread rate is evaluated in a manually chosen region (when the tip seems to move at a constant rate). Note that in this case, the flame spread rate of the flame tip is almost double of that of the flame base and the flame length increases at least until the flame tip reaches the end of the camera view. As observed in the previous case, when the flame tip reaches the open end of the sample, it accelerates and the two flames on both sides of the sample merge. Eventually, the sample is fully consumed and the flame extinguishes.

As shown in Fig. 10, the flame at this flow speed (28 cm/s) appears much more luminous (confirmed verbally by crew) and sootier than that in low flow speeds (Fig. 8). Blue flame is only observed near the upstream base region. At high flow speeds, the flame is stronger and longer. The high flame temperature and increased rate of pyrolysis promotes the formation of soot throughout the combustion zone. The blue flame layer is less visible compared to the highly luminous yellow sooty part of the flames and hence not completely captured by the camera.

### 3.3. Effects of flow confinement

To understand the effects of flow confinement, the steady state flame profiles at different inter-baffle distances (and with no baffles) are compared in Fig. 11. Here, we compare tests with the same imposed flow speed of 6 cm/s and with black baffles (if used). When the confinement varies from no baffles (the full duct width, equivalent to $D = 7.6$ cm) to the most confined case ($D = 2.0$ cm), flame length first increases and then decreases. The maximum flame length occurs at around $D = 4.0$ cm. When the inter-baffle distance further decreases to $D = 1.0$ cm, the flame quenches immediately after ignition energy is removed. Post-burn sample indicated that the flame never spread past the ignition wire (the sample burn length is less than 0.8 cm).

Note that in the case with no baffles, the sample was installed on the sample carrier (Fig. 2b) alone. The two sides of the sample were exposed directly to the interior of the flow duct (left side in Fig. 11) and to the front window (right side) respectively. The interior of the flow duct is painted black and its radiation property, although not measured, is expected to be close to a black surface. The front window was made of visibly transparent polycarbonate.

Also note that when the flame is small and weak at very small inter-baffle distances (e.g., $D = 2.0$ cm), the camera is struggling with white balance and the videos show unrealistic colors of the flames. The apparent colors would change between one video frame and the next. However, the ISS crew reported true flame color during the burns to confirm/correct the video displayed.

Flame contours and flame center profiles are also compared in Fig. 11. The flames at different baffle setups seem to have similar flame shapes (except with different flame lengths). The standoff distance of the flame tip varies between 0.4 - 0.7 cm depending on the flame lengths.

The flame spread rates and flame lengths at different inter-baffle distances are compared in Fig. 12. Note that as discussed in Section 2.2, flames may encounter different flow speeds at different baffle setups even when the same flow is imposed at the duct inlet. The flow velocities obtained in the pre-flight flow characterization ($U_c$, measured at center of the confined space) are labeled in Fig. 12 for reference. Also note that the variation of these measured flow speeds between different baffle setups might be larger than the variation of the actual flow encountered by the flame (see Fig. 4).

Both flame length and flame spread rate exhibit non-monotonic trends when the inter-baffle distance decreases. When the confinement increases from $D = 7.6$ cm (no baffle case) to $D = 4.0$ cm, the flame spread rate increases by a factor of ~1.62 for the black anodized aluminum baffles. Compared with $D = 5.0$ cm, the test with $D = 4.0$ cm has a larger flame length and flame spread rate, despite

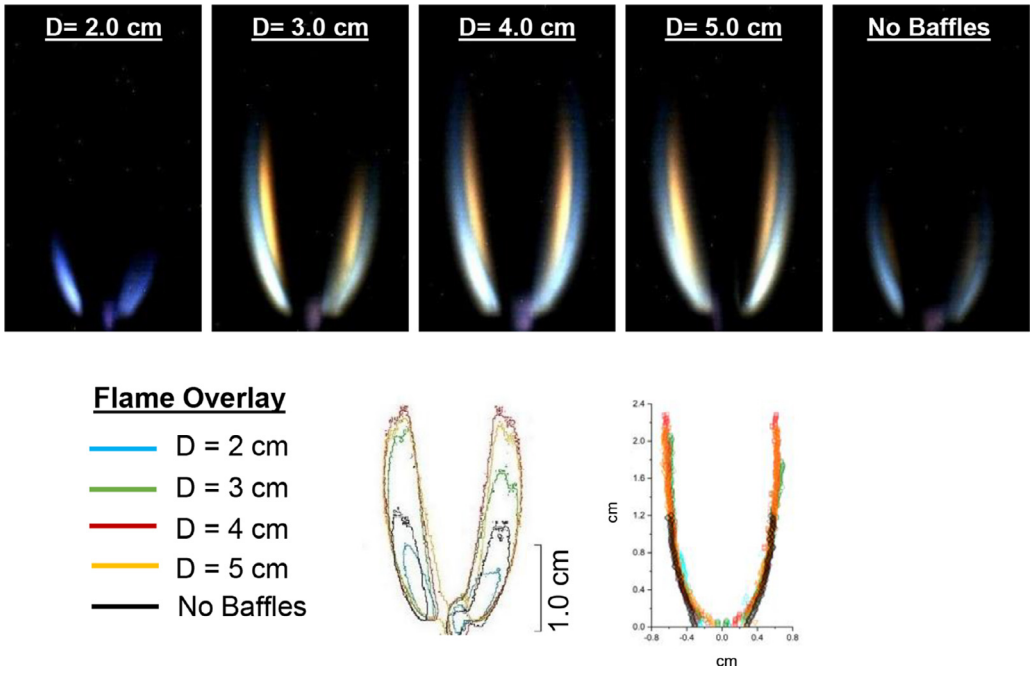


**Fig. 11.** [Top] Comparisons of steady flame profiles at different flow confined conditions. Baffle types (if used): black anodized aluminum baffles. Imposed flow speed: 6 cm/s. [Bottom] Overlay of tracked flame outer edge and flame center profile for all five tests. In the case with no baffles, the flame is between a black duct wall (left side in the figure) and a transparent polycarbonate window (right side in the figure).

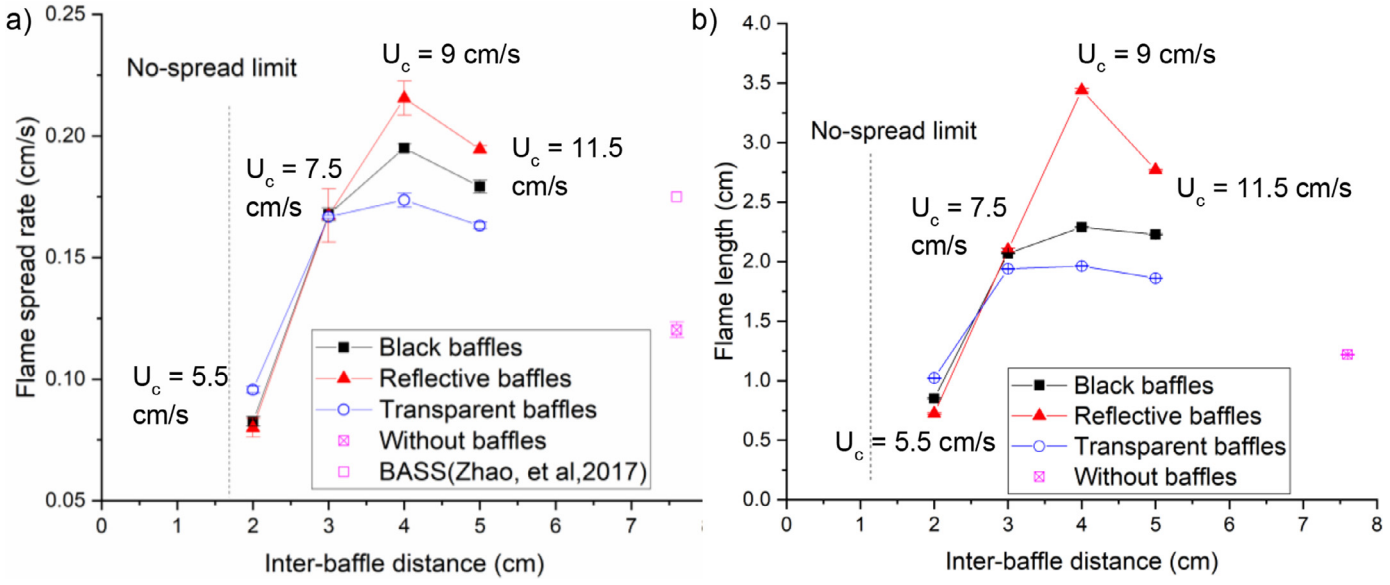


**Fig. 12.** Flame spread rates and flame length at different inter-baffle distances. Imposed flow speed: 6 cm/s. Maximum flow speeds in the confined region (based on the pre-flight cold flow measurements) are labeled for each baffle setup. Error bar denotes the 95% confidence intervals of the measurements.

having a slightly lower measured local flow speed. This demonstrates the effects of flow acceleration due to thermal expansion during confined combustion. Compared with the inversely proportional relationship between spread rate and tunnel height ($V_f \sim 1/D$) predicted by Li et al. [10], the spread rate increases slower when D decreases, due to a decreasing local flow rates. For the reflective highly polished aluminum baffles, the increases in spread rate and flame length are even higher due to the additional radiative heat feedback reflected from the baffles (will be discussed further below).

As predicted by Li et al. [10], the optimal inter-baffle distance for the flame spread occurs at $D = 4.0$ cm. The spread rate and flame length reach the maximum values for all baffle types. Below this inter-baffle distance, the flame spread rate decreases with the inter-baffle distance. The decreasing local flow speeds encountered by the flame certainly contributes to the decreasing flame spread rate. Other effects that may result in the decreased flame spread rate at small-baffle distances include oxygen starvation and conductive heat loss to the baffles [10]. At $D = 1.0$ cm, self-sustained flame was not achieved and flames extinguished after ignition power was off for any baffle types. Once again, at this small baffle distance, local flow near the sample surface is greatly reduced by flow viscosity. In addition, flame can act as a pseudo-body and further prevents the flow from entering the inter-baffle region [1]. It

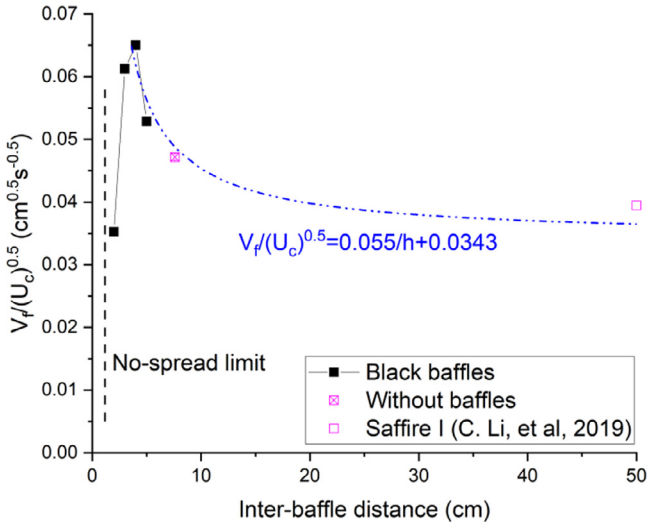


**Fig. 13.** Flame spread rate $\boldsymbol{V_f/\sqrt{U_c}}$ at different flow confinement in microgravity.

is suspected that the flame extinction at this baffle configuration is caused by the low flow speed in the combustion region. This might also explain the identical no-spread limits for different baffle types shown in Figs. 7 and 12.

Flame spread rate from the previous BASS experiment is also included in Fig. 12. This data was obtained using the same sample material in similar environmental conditions (1atm, 21% $O_2$) and with a slightly lower concurrent flow rate at 5 cm/s. Compared with the case with no baffles in this work, the spread rate in previous BASS is ~ 42% higher. This difference in flame spread rates might be due to a combination of various reasons, one being the different widths of the sample frames used in previous and current tests (3.6 cm vs 6.1 cm, respectively). The wider sample frame used in this work is likely to introduce more heat loss and to reduce side oxygen transport to the combustion zone, both of which weaken the flame. In addition, in this work, the sample frame is closed at the upstream end and open at the downstream end of the sample (Fig. 2b). This is opposite to the previous BASS experiments. The upstream portion of the sample frame can potentially lead to a lower flow speed (due to the viscous effects) near the sample surface compared to BASS. Last, there were other hardware differences between the previous BASS and current work. For example, the sample orientation was rotated 90-degrees in the duct and the sample holder mechanism was slightly different.

For concurrent-flow flame spread over thin solid fuels in microgravity, previous work has shown that the flame spread rate is proportional to $\sqrt{U_\infty}$ [31]. To take into considerations the different flow speeds in the confined region at different baffle configurations, adjusted flame spread rate $\boldsymbol{V_f/\sqrt{U_c}}$ is plotted against the inter-baffle distance in Fig. 13 using black baffle data. Note that data from a recent large-scale microgravity experiment Saffire is also included. In Saffire [6,7], the same sample material (SIBAL) was burned in a large flow duct with duct height ~ 50 cm in a concurrent flow 20 cm/s.

At large inter-baffle distances, $D > 4.0$ cm, $\boldsymbol{V_f/\sqrt{U_c}}$ is shown to be inversely proportional to D, consistent with the prediction in previous numerical work [10]. Assuming the volumetric expansion of the combusting gases are similar in all tests, the flow acceleration along the stream direction is inversely proportional to the cross-sectional area (or the inter-baffle distance). This further implies the stronger flame in the confined space is caused by the flow acceleration due to thermal expansion.

At small inter-baffle distances, $D < 4.0$ cm, Fig. 13 shows that the flame spread rates, after being adjusted by the local flow speeds, still decrease with D. This suggests that the oxygen starvation plays a role at these confined conditions. Assuming the combustion is limited by the oxygen entering the inter-baffle region, for steady flame spread with complete combustion, $V_f \rho_s \tau = U_c \rho_{air} D Y_{O2} r$. Here, $\rho_s$ and $\rho_{air}$ are the density of the solid fuel and air respectively, $\tau$ is the thickness of the solid fuel, $Y_{O2}$ is the oxygen mass fraction of the air, and $r$ is the stoichiometric fuel to oxygen ratio. Based on this, $V_f/U_c$ is expected to be proportional to D. In this work, when D increases from 2 cm to 3 cm, $V_f/U_c$ increases by 49% for black baffles.

### 3.4. Effects of radiation interaction

The flame profiles for different baffle types are compared in Fig. 14. In these cases, the inter-baffle distances are 4.0 cm and the imposed flow speed is 6 cm/s. Among the three cases, flame is significantly longer when the reflective baffles are used, as expected. During the burning process, a portion of the combustion heat is lost to the environment through radiation. The reflective baffles help to re-direct radiation back to the sample and the gaseous flame. On the other hand, a significantly higher portion of radiation penetrates or is absorbed by the transparent polycarbonate and black anodized aluminum baffles. Compared with the transparent baffles, the flame is slightly longer for the black baffles. During the burning process, temperature of the baffles may increase, resulting in increased surface radiation emission. The longer flame observed for the black baffles is likely due to the combination of a slightly higher radiation reflection and emission than transparent baffles.

In Fig. 12, it is noticed that at small inter-baffle distances (e.g., $D < 3.0$ cm), the flame spread rates for black and reflective baffles are similar but are different from those for transparent baffles. To further compare the differences caused by the baffle types, the ratios of the spread rates of the reflective and black baffles to the spread rate of the transparent baffles are shown in Fig. 15.

In general, the additional radiation feedback from the reflective baffle results in a higher flame spread rate compared with the black and transparent baffles. This effect is most prominent near the optimal inter-baffle distance, $D = 4.0$ cm. At small baffle distances (e.g., $D = 3.0$ cm), the flame spread rates for different baffles are almost identical. This further suggests that at these confined conditions, the combustion is limited by the oxygen supplied to the inter-baffle region.

Note that at the minimum inter-baffle distance for which a flame spreads, $D = 2.0$ cm, the flame spread rate for the transparent baffles is slightly higher than other baffle types. This indicates that at this inter-baffle distance, the flame is close enough to the baffles such that conductive heat loss contributes to the decrease of the flame spread rate [8,9]. Compared with the polycarbonate, the polished and anodized aluminum baffles have significantly larger thermal conductivity (200 vs. 0.2 W/m/K) and larger volumetric heat capacity ($\rho \cdot C_p$ ~ 2.46 vs. 1.44 J/cm$^3$/K), and are therefore expected to introduce more heat loss from the flame zone.

The total heat release of the SIBAL sample is estimated at ~5.24 kJ, using the heat of combustion of the cotton at $\Delta h_c$=17.44 kJ/g [32]. For the aluminum baffles to have an average temperature rise of 10 K, assuming no heat loss from the baffle surfaces, the heat loss from the flame to the baffles is estimated at ~0.66 kJ, ~12% of the total combustion heat release. While the baffle temperature was not measured in the ISS experiments, the heat loss to the baffles is expected to play a role in the flame spread processes at low inter-baffle distances when the baffles are in the close proximity of the flame.

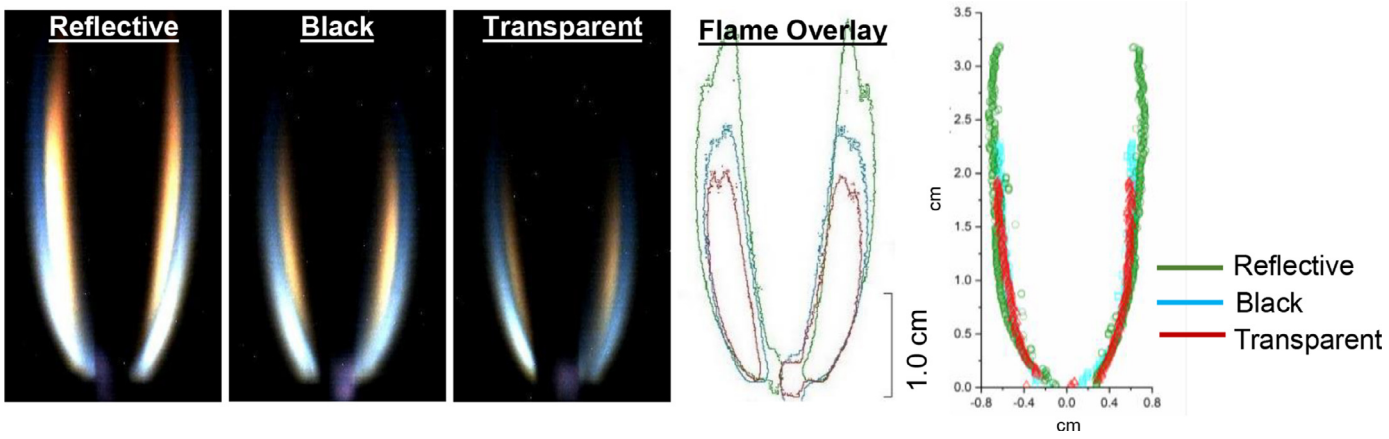


**Fig. 14.** [Left] Comparisons of steady flame profiles between different baffle types. Baffle distance $D = 4.0$ cm. Imposed flow speed: 6 cm/s. [Right] Overlay of tracked flame outer edge and flame center profile for all three tests.

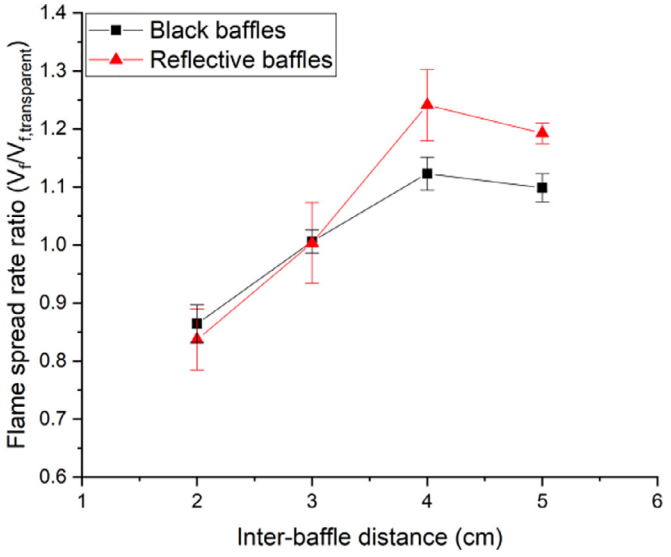


**Fig. 15.** Comparisons of flame spread rate between different baffle types. The spread rate of transparent baffles is used as reference and its value in this plot is unity at all inter-baffle distances.

## 4. Conclusion

This work leverages the unique long-duration microgravity environment aboard the International Space Station (ISS). A series of purely-forced concurrent flow flame spread experiments were performed to study the effects of confinement on burning characteristics of solid materials. Thin cotton-fiberglass blend fabrics were burned in a small flow duct. Confinement is introduced using two baffles with adjustable distance between 1 and 5 cm installed parallel to the sample, one on each side symmetrically. Three types of baffles: black anodized aluminum, reflective polished aluminum, and transparent polycarbonate were used to simulate different radiative boundary conditions from the surrounding walls. While the imposed flow speeds are controlled (ranging from 5 to 28 cm/s), the flow that enters the confined region varies for different baffle setups. Flow characterization was performed prior to the ISS operations to provide information on the cold flow profiles in the confined region where the flame resides.

By varying the flow conditions and confinement levels, flames exhibit different spreading modes: no spreading, steady spreading, and accelerating spreading. Profiles and transient development processes of both accelerating and steady flames are examined and presented through high-resolution images. Main findings are as follows:

(1) For low tested flow speeds (<17 cm/s) and all baffle types, steady state flame spread is reached and a limiting flame length and constant spread rate are observed. In addition, there exists a quenching inter-baffle distance below which the flame failed to spread.

(2) For large tested flow speeds (>17 cm/s), the flame continually grows throughout the test, except when the baffle distance is near the quenching distance. It is possible that the sample size and flow duct used in this work are too small for the flame to reach steady state in these conditions. In other words, the boundary of the steady and accelerating flames observed in this work may be specific to the experimental hardware.

(3) For cases where steady flame spread was observed, the results confirm the previously predicted non-monotonic effects of flow confinement on the burning characteristics. There exists an optimal inter-baffle distance for flame length and spread rate. Above this optimal distance, the confinement affects the burning mainly through the thermal expansion during combustion, which accelerates the flow and enhances the conductive heat feedback to the sample. This results in a higher flame spread rate. When the inter-baffle distance is smaller than the optimal distance, the flame suffers from the oxygen starvation and additional heat loss to the adjacent baffles. These weaken the flame and decrease the flame spread rate.

(4) In this work, the optimal inter-baffle distance for flame spread is 4 cm, consistent with the previous model prediction. However, considering this optimal confined condition is resulted from the combined effects of flow acceleration during combustion, oxygen limitation, and heat loss to the surrounding walls, in reality, this critical inter-baffle distance can vary with many factors. These factors include, for example, material of the solid combustible, thermal physical properties and radiative surface treatment of the duct walls, width and configuration of the flow duct, and of course, buoyancy effects.

(5) The reflective aluminum baffles in general have the strongest flame (highest spread rate and longest length) and the transparent polycarbonate baffles have the weakest flames. This effect is most prominent near the optimal inter-baffle distance. The trend reverses at quenching for small inter-baffle distances as the transparent baffles conduct the least heat away from the flame among the three baffle types.

(6) The experiments in this work provide a rich data that can be used for benchmarking and validation for future numerical model and theory development.

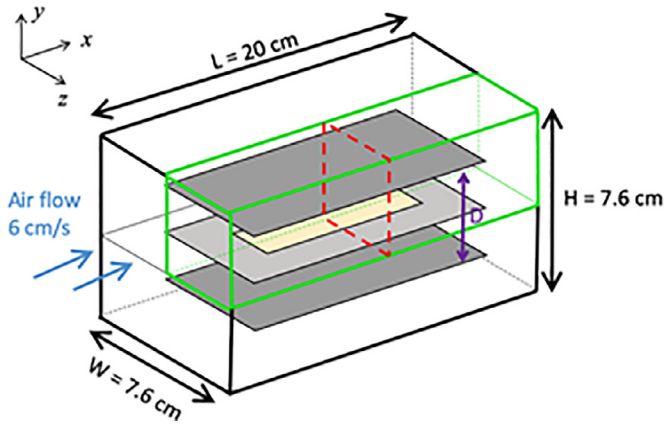


**Fig. A.1.** CFD cold-flow model configuration.

## Declaration of Competing Interest

None.


## Acknowledgments

This research is co-sponsored by the National Science Foundation and Center for the Advancement of Science in Space (CASIS) under grant number CBET-1740478. Hardware modifications for Confined Combustion and the original BASS hardware were performed by ZIN Technologies. The science team received tremendous support during operations from NASA Glenn Research Center, Marshall Spaceflight Center, and ZIN Technologies, and especially Emily Griffin, Steve Lawn, Russell Valentine, Beth Curtis, Chris Rogers, Wendell Booth, Michael Hall, and the Microgravity Science Glovebox team. We would also like to express our immense appreciation to our lab partners in space, ISS crew members Christina Koch, Jessica Meir, Andrew Morgan, and Luca Parmitano for supporting and conducting the microgravity experiments aboard the ISS.


## Appendix

To help characterize the flow profile in the experiment hardware, the steady cold-flow (with no combustion) profile is

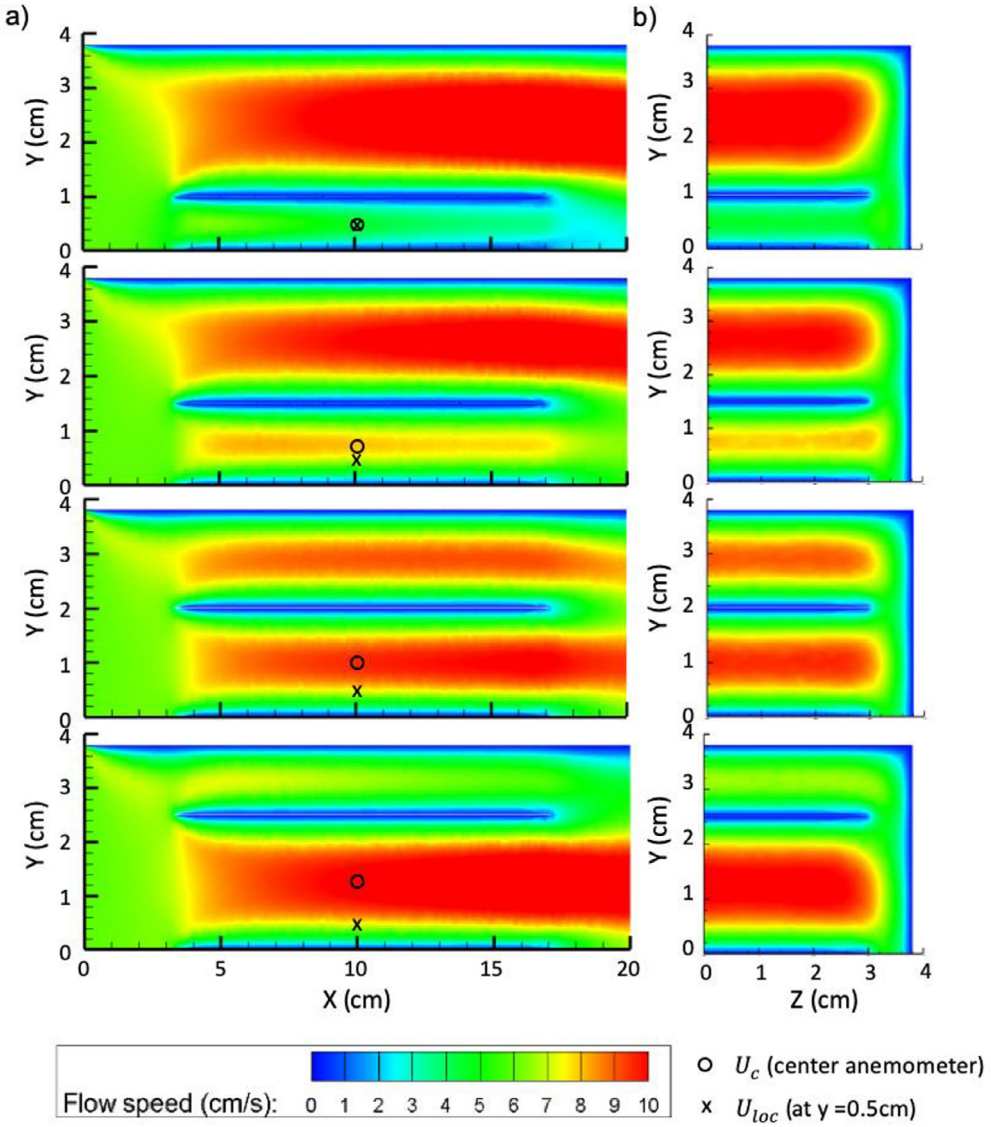


**Fig. A.2.** Flow velocity profiles for different baffle configurations. a) u-velocity on the center-plane ($z = 0$). b) u-velocity on the mid cross-section plane ($x = 10$ cm, marked by the red dash line in Fig. A.1). From top to bottom, $D = 2$, 3, 4, and 5 cm.

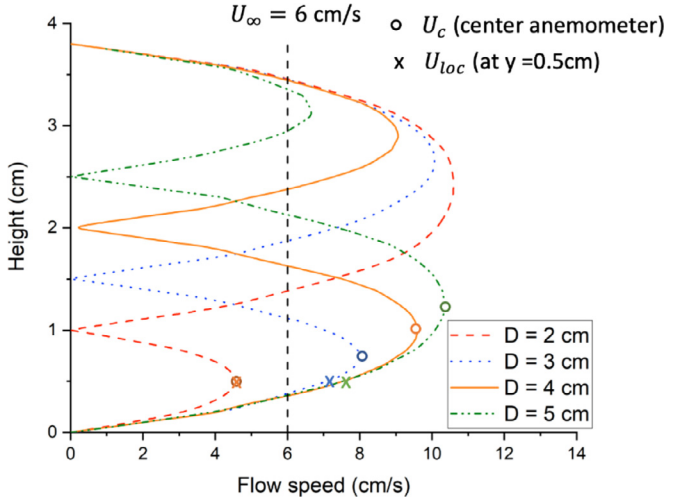


**Fig. A.3.** Flow velocity distribution along the duct height at the center of the flow duct ($x$ = 10 cm, $z$ = 0).

simulated using ANSYS Fluent. The configuration is shown in Fig. A.1. Three parallel plates (simulating the baffles and the sample card in the ISS experiments) are positioned in the center of a flow duct. The dimensions of the flow duct and the plates are the same as those used in the microgravity experiment. Four different inter-baffle distances ($D$ = 2, 3, 4, 5 cm) are simulated. Because of the symmetric nature of the geometry, only a quarter of the domain (marked by the green box in Fig. A.1) is simulated. Uniform flow of 6 cm/s is imposed at the inlet of the flow duct. The working fluid is air at 300 K and 1 atm. Constant gas density and viscosity are assumed.

The simulation results of different inter-baffle distances are compared in Figs. A.2 and A.3. Figures A.2a and A.2b show the steady-state streamwise flow velocity (i.e., the u-velocity) on the center-plane ($z$ = 0) and on the mid cross-section of the flow duct ($x$ = 10 cm, marked by the red dash line in Fig. A.1) respectively. Fig. A.3 shows the u-velocity along the duct height on the mid-plane at the center of the flow duct ($x$ = 10 cm, $z$ = 0). When encountering the baffle and the sample card, the flow is separated into two flow pathways in the simulated domain: the pathway between the baffle and the duct ceiling ($y = D/2$ ~ 3.8 cm, or pathway I in Fig. 5) and the pathway between the sample card and the baffle ($y$ = 0 ~ D/2, or pathway II in Fig. 5). The simulation results show that the flow in pathway II decreases when the inter-baffle distance decreases, consistent with the pre-flight flow measurements. In the pre-flight flow characterization, an anemometer is placed at the center of the flow duct. Simulated local flow speeds at this location (marked by hollow circles in Figs. A.2 and A.3) match the measurement reasonably well (within 16% difference). Local flow speeds at the estimated flame height location (marked by black crosses in Figs. A.2 and A.3) are also evaluated using the simulation results.

## References


[1] A. Vetturini, W. Cui, Y.-T.T. Liao, S. Olson, P. Ferkul, Flame spread over ultra-thin solids: effect of area density and concurrent-opposed spread reversal phenomenon, Fire Technol 56 (2020) 91–111.

[2] S.L. Olson, P.V. Ferkul, J.S. T'ien, Near-limit flame spread over a thin solid fuel in microgravity, Symp. Int. Combust. 22 (1989) 1213–1222.

[3] A.F. Osorio, K. Mizutani, C. Fernandez-Pello, O. Fujita, Microgravity flammability limits of ETFE insulated wires exposed to external radiation, Proc. Combust. Inst. 35 (2015) 2683–2689.

[4] H.D. Ross, Basics of microgravity combustion, in: H.D. Ross (Ed.), Microgravity Combustion: Fire in Free Fall, Eds, Academic press, London (2011), pp. 22–23.

[5] X. Zhao, Y.-T.T. Liao, M.C. Johnston, J.S. T'ien, P.V. Ferkul, S.L. Olson, Concurrent flame growth, spread, and quenching over composite fabric samples in low speed purely forced flow in microgravity, Proc. Combust. Inst. 36 (2017) 2971–2978.

[6] D.L. Urban, P. Ferkul, S. Olson, G. Ruff, J. Easton, J.S. T'ien, Y.-T.T. Liao, C. Li, C. Fernandez-Pello, J. Torero, G. Legros, C. Eigenbrod, N. Smirnov, O. Fujita, S. Rouvreau, B. Toth, G. Jomaas, Flame spread: effects of microgravity and scale, Combust. Flame 199 (2019) 168–182.

[7] C. Li, Y.-T.T. Liao, J.S. T'ien, D.L. Urban, P. Ferkul, S. Olson, G.A. Ruff, J. Easton, Transient flame growth and spread processes over a large solid fabric in concurrent low-speed flows in microgravity – model versus experiment, Proc. Combust. Inst. (2018) 4163–4171.

[8] Y. Li, Y. Liao, P. Ferkul, Concurrent-flow flame spread over a thin solid in a narrow confined space in microgravity, Intl. Mech. Eng. Congress & Expo. (2019) 2019–11908 paper.

[9] H.-Y. Shih, J.S. T'ien, Modeling wall influence on solid-fuel flame spread in a flow tunnel, 35th Aerospace Science Meeting & Exhibition (1997), pp. 97–0236. paper.

[10] Y. Li, Y.-T.T. Liao, P. Ferkul, Numerical study of the effects of confinement on concurrent-flow flame spread in microgravity, J. Heat Trans.-T. ASME 142 (2020) 11301 paper.

[11] Y. Nakamura, T. Kashiwagi, K.B. McGrattan, H.R. Baum, Enclosure effects on flame spread over solid fuels in microgravity, Combust. Flame 130 (2002) 307–321.

[12] S.L. Olson, T. Kashiwagi, O. Fujita, M. Kikuchi, K. Ito, Experimental observations of spot radiative ignition and subsequent three-dimensional flame spread over thin cellulose fuels, Combust. Flame 125 (2001) 852–864.

[13] H.-Y. Shih, H.-C. Wu, An experimental study of upward flame spread and interactions over multiple solid fuels, J. Fire Sci 26 (2008) 435–453.

[14] B. Comas, A. Carmona, T. Pujol, Experimental study of the channel effect on the flame spread over thin solid fuels, Fire Safety J 71 (2015) 162–173.

[15] H. Zhu, G. Zhu, Y. Gao, G. Zhao, Experimental studies on the effects of spacing on upward flame spread over thin PMMA, Fire Technol 53 (2017) 673–693.

[16] Author S. Olson, Low-gravity flames, in: C. Baukal Jr., A. Agarwal, S. Olson, M. Gollner, T. Jacobs, M. Vaccari (Eds.), A Gallery of Combustion and Fire, Eds., Cambridge University Press (2020), pp. 74–106.

[17] C. Fernandez-Pello, Upward laminar flame spread under the influence of externally applied thermal radiation, Combust. Sci. Technol. 17 (1977) 87–98.

[18] M. Thomsen, X. Huang, C. Fernandez-Pello, D.L. Urban, G.A. Ruff, Concurrent flame spread over externally heated Nomex under mixed convection flow, Proc. Combust. Inst. 37 (2019) 3801–3808.

[19] J. Pepper, F. Miller, S. Olson, I. Wichman, A study of the effectiveness of a narrow channel apparatus in simulating microgravity flame spread over thin fuels, 42nd International Conference on Environment System (2012), pp. 2012–3493. paper.

[20] S. Hossain, I.S. Wichman, G.W. Sidebotham, S.L. Olson, F.J. Miller, Influence of gap height and flow field on global stoichiometry and heat losses during opposed flow flame spread over thin fuels in simulated microgravity, Combust. Flame 193 (2018) 133–144.

[21] T. Matsuoka, K. Nakashima, T. Yamazaki, Y. Nakamura, Geometrical effects of a narrow channel on flame spread in an opposed flow, Combust. Sci. Technol. 190 (2018) 409–424.

[22] S. Hossain, I.S. Wichman, F.J. Miller, S.L. Olson, Opposed flow flame spread over thermally thick solid fuels: buoyant flow suppression, stretch rate theory, and the regressive burning Regime, Combust. Flame 219 (2020) 57–69.

[23] S.L. Olson, F.J. Miller, S. Jahangirian, I.S. Wichman, Flame spread over thin fuels in actual and simulated microgravity conditions, Combust. Flame 156 (2009) 1214–1226.

[24] S.L. Olson, P.V. Ferkul, S. Bhattacharjee, F.J. Miller, J.S. T'ien, I. Wichman, Results from On-board CSA-CP and CDM sensor readings, 45th International Conference on Environment System (2015), pp. 2015–2196. paper.

[25] E.K. Plyler, C.J. Humphreys, Infrared emission spectra of flames, J. Res. Natl. Bur. Stand. 40 (1948) 449–456.

[26] C.O. Ayieko, R.J. Musembi, A.A. Ogacho, B.O. Aduda, B.M. Muthoka, P.K. Jain, Controlled texturing of aluminum sheet for solar energy applications, Adv. Mater. Phys. Chem. 5 (2015) 458–466.

[27] J.L. Marshall, P. Williams, J.-P. Rheault, T. Prochaska, R.D. Allen, D.L. DePoy, Characterization of the reflectivity of various black materials, Ground-based and Airborne Instrumentation for Astronomy, SPIE 9147, 2014 Paper 91474F.

[28] CovestroOptical properties of Makrolon and Apec, Report No. COV00072203, Covestro Deutschland AG, Leverkusen, Germany, 2017.

[29] Sheffield PlasticsProduct Data: Makrolon UC Sheet, Report No. MAKUC 0310, Sheffield Plastics, Sheffield USA, 2010.

[30] J.P.D. Plessis, M.R. Collins, A new definition for laminar flow entrance lengths of straight ducts, 1992, N&O J 9 (2012) 11–16.

[31] C. Li, Y.-T. Liao, Effects of ambient conditions on concurrent-flow flame spread over a wide thin solid in microgravity, Proc. Combust. Inst. (2020), doi:10.1016/j.proci.2020.05.011.

[32] I.A. Tarchevsky, G.N. Marchenko, Thermodynamic properties of cellulose and its satellites, Cellulose: Biosynthesis and Structure, Heidelberger Lehrtexte WirtschaftswissenschaftenSpringer, Berlin (1991), pp. 210–220.